Ground ice estimation in permafrost samples using industrial Computed Tomography and Multi-Sensor Core Logging and comparison to destructive measurements

Mahya Roustaei [1,2*], Joel Pumple [1], Jordan Harvey [1], and Duane Froese [1,*]

[1] Department of Earth and Atmospheric Sciences, University of Alberta, Edmonton, Canada
[2] UGent Geotechnical Institute~~Geotechnics Laboratory~~, Ghent University, Technologiepark 68, 9052 Zwijnaarde, Belgium

Correspondence to: Mahya Roustaei (m~~roustae@ualberta.ca~~ahya.roustaei@ugent.be) or Duane Froese (duane.froese@ualberta.ca)

9 **Abstract.**

10 Permafrost contains a variety of ground ice types (e.g., pore, segregated, intrusive, vein, or massive ice) that have a diversity

11 of cryotextures which organise to form distinctive cryostructures. The distribution and abundance of those ground ice types

12 determines the potential for thaw subsidence and terrain effects of permafrost landscapes. Analysis of permafrost samples

13 allows improved understanding of ground ice formation, internal and external permafrost processes, and improved tools to

14 predict thaw settlement and consolidation. However, most methods to characterise permafrost are destructive and of low

15 resolution. Here, some of the limitations of traditional destructive methods are overcome using an industrial Computed

16 Tomography scanner (CT). We use this laboratory-based method to systematically characterize five permafrost samples. We

17 visualise cryostructures, measure frozen bulk density, and estimate volumetric and excess ice contents non-destructively and

18 compare these results with traditional destructive analyses at similar spatial scales.

19 The results show strong agreement between traditional destructive analyses (RMSE's for density, volumetric ice, and excess

20 ice contents are 0.12 g/cm3, 3% and 6%, respectively) as well as recent developments using a Multi-Sensor Core Logger

21 (MSCL) (RMSE's for density and volumetric ice contents are 0.08 g/cm3 and 7%, respectively). These results demonstrate

22 that these non-destructive approaches can produce consistent results, and provide the added benefit of archiving images and

23 enhancing digital permafrost datasets. Development of standardised and interoperable methods for permafrost characterization

24 has the potential to build more robust permafrost datasets and strengthen efforts to understand future thaw trajectories of

25 permafrost landscapes.

1 Introduction

Permafrost is rock or soil that has remained below 0°C for at least two consecutive years. Within permafrost, several different types of ground ice can form: pore ice within the void spaces between soil or rock particles; segregation ice as distinct lenses formed through migration of water within permafrost; aggradational ice, a type of segregation ice, that forms as the permafrost table rises; vein or wedge ice that forms within thermal contraction cracks; intrusive ice that forms when water is injected under pressure; or massive ice that refers to relatively pure bodies of ice within permafrost (Subcommittee on Permafrost., 1988). These differing types of ground ice have distinctive associations of cryotextures, which refer to the appearance and characteristics of ice crystals, gas bubbles and their interfaces with soil particles at a more microscopic scale; and cryostructures which refer to the three-dimensional patterns and arrangements of ice bodies within the frozen ground (such as layered, lenticular, or reticulate patterns) (Murton and French, 1994; French and Shur, 2010). Taken together, these ice-related features help identify the genesis of perennially frozen sediments and can provide insights into the conditions under which the permafrost formed, which can aid in understanding potential ground ice distribution. Of particular importance is excess ice – or ground ice that exceeds the natural pore volume that the sediment would have under unfrozen conditions (Brown et al., 1997; Zhang et al., 1999; Cai et al., 2020; Van Everdingen, 1998). When excess ice melts, it causes thaw settlement and ground subsidence, making its quantification increasingly critical as warming temperatures degrade permafrost across permafrost regions (e.g. Kokelj et al., 2024). Projections of widespread permafrost thaw by the end of this century (e.g. Cai et al., 2020) highlight an urgent need for standardised methods to measure and map excess ice distribution to better predict future landscape changes.

Cryostructural approaches to ground ice classification aim to understand permafrost development by systematically analyzing the shape, size, and spatial patterns of ice inclusions in frozen ground. These methods contrast with more commonly used engineering-focused descriptive systems, which rely primarily on visual descriptions and simple field tests, such as thawing samples to observe supernatant water content. While the descriptive approach provides practical field-based classifications useful for engineering applications, the cryostructural approach offers more process-based insight into permafrost formation processes and potential ground ice distribution, which is increasingly important for predicting thaw settlement and landscape response to climate warming (French and Shur 2010).

Cryostructural approaches to ground ice classification, building on Russian literature, particularly Katasonov's (1969, 1978) cryofacies methods, focus on understanding permafrost genesis and development through systematic analysis of the shape, size and spatial patterns of ice inclusions in frozen ground. This approach contrasts with the more commonly used North American engineering-focused descriptive systems developed by Pihlainen and Johnston (1963) and Johnston (1981), which rely primarily on visual descriptions and simple field tests, such as thawing samples to observe supernatant water content similar to the method described in Kokelj and Burn (2003). While the descriptive approach provides practical field-based

Traditional approaches to permafrost characterization , whether using more descriptive engineering-oriented approaches (Pihlainen and Johnston, 1963; Johnston, 1981) or more detailed cryostructural classifications (Murton and French, 1994; French and Shur, 2010), rely heavily on visual description of exposures and cores (Kanevskiy et al., 2011; Stephani et al., 2014). While these approaches have advanced our understanding of permafrost, they require substantial experience of the analyst, and are difficult to standardise. Quantitative methods typically require destruction of samples to measure ice and moisture contents, which works well for ice-rich mineral soils but presents challenges for organic-rich materials where water may be retained in thawed samples. These limitations have driven the development of non-destructive methods like Computed Tomography (CT) scanning that can systematically analyse intact frozen cores, providing standardised, quantitative data on ground ice while preserving samples for additional analyses (Calmels and Allard 2004, 2008, Calmels et al., 2010). This approach offers the potential to better understand permafrost formation, internal structure, and likely response to thaw while developing more consistent and interoperable methods applicable across different permafrost materials.

Micro-computed tomography (µCT), which offers much higher spatial resolution than conventional CT, has emerged as a promising solution to the limitations of traditional permafrost characterization methods since the pioneering work of Calmels and Allard (2004, 2008), who demonstrated its utility for measuring ice and gas contents in permafrost and linking these to processes of ground ice formation. Subsequent studies have expanded the application of µCT scanning to examine cryostructures (Calmels et al., 2010; Fan et al., 2021), excess ice (Lapalme et al., 2017), soil degradation in freeze-thaw cycles (Nguyen et al., 2019; Wang et al., 2018, 2017; Roustaei et al., 2022, Roustaei et al., 2024), quantification of micro-lenticular ice lens formation (Darrow and Lieblappen, 2020), unfrozen water content (Roustaei et al., 2022), soil-ice relations (Torrance et al., 2008), and permafrost composition (Nitzbon et al., 2022).

HoweverAlthough the method has developed, , despite these advances, there have been few systematic comparisons of high-resolution µCT scanning (< 100 µm) with established methods for differentiating excess ice from pore ice across different permafrost materials. µCT typically offers very high spatial resolution (down to a few microns) for small samples, while industrial CT provides a balance of higher power and the ability to scan larger samples at slightly lower resolution, and medical CT is generally optimized for human-sized imaging at lower resolution and power. This study addresses this gap by using industrial CT scanning, which offers higher peak power and resolution than medical CT scanners, to analyse five different permafrost cores representing a range of typical properties (e.g., density and ice contents). We develop a new approach using an internal water standard to calibrate linear attenuation coefficients to real density values, and systematically compare CT-derived measurements of frozen bulk density, excess ice, and volumetric ice contents with both destructive physical

Commented [MR1]: Check the sentence from ref, reformulat the paragraph and delete North america

Commented [MR2]: Delete the refs from refs

Commented [MR3]: Add more CT refs

Commented [MR4R3]: Add one line about the diffrence of and micro CT and then make sure all the refs are using micro

Commented [MR5]: Chang this to say still no study has systematically addresse ...

Commented [MR6]: What is the diffrence of industrial, ct an micro???

Commented [MR7]: What properties?

90 measurements and Multi-Sensor Core Logging (MSCL). ~~results from Pumple et al. (2023).~~ We include a sensitivity analysis
91 to examine how spatial resolution affects excess ice estimation. While our sample set does not capture the full heterogeneity
92 of permafrost materials and ground ice abundance, it provides a rigorous test of CT methods for quantifying ground ice in
93 common permafrost materials~~, with the goal of developing more robust and standardised approaches for permafrost~~
94 ~~characterization and mapping.~~.

2 Methods and Materials

2.1 Site and sampling

101 Five cores were investigated in this study, each representing common materials encountered in permafrost regions, such as silt
102 (ice-poor and ice-rich), peat, silty peat, and diamicton (a coarser, mixed-grain material), and containing a relatively simple
103 vertical cryostratigraphy to minimize the impact of lateral heterogeneity (Table 1). Minimizing lateral heterogeneity is
104 important because such variations can introduce noise when comparing multiple data acquisition methods applied to different,
105 but nearby, sample volumes within the same core (Figure 1). This consideration and its implications are explained further by
106 Pumple et al. (2024), who discuss how variations in measured densities of permafrost cores may reflect real heterogeneities in
107 physical properties or artifacts introduced due to core preparation or mounting of frozen materials. ~~Lateral heterogeneity would~~
108 ~~cause noise in our results when comparing multiple data acquisition methods within the same material but not identical sample~~
109 ~~volumes (Figure 1). This effort is explained further by Pumple et al. (2024).~~
110 These cores were collected as ~~a result of~~during two separate field campaigns ~~during the summers of~~in 2013 and 2019 with
111 some cores being collected in southwestern Yukon along the Alaska Hwy and other in Central Yukon along the Dempster
112 Hwy. All cores were collected in a sub-arcitic setting. Following extraction, the cores were bagged, labelled and stored at
113 subzero temperatures via a pre chilled cooler and quickly transported to the field base where a chest freezer was present. The
114 chest full of cores was then transported to the Permafrost ArChives Science (PACS) Laboratory and ~~The samples were then~~
115 archived into ~~the PACS Lab~~ walk-in archive freezer space. Samples were prepared for two different stages; non-destructive
116 scans and destructive physical measurements. ~~We took considerations in both stages to ensure the destructive and non-~~
117 ~~destructive results were comparable.~~ As such for the non-destructive scans, physical cores were cut in half and run through all

Commented [MR8]: This is not clear, which effort? lateral heterogeneities? then joint this reference to the previous line

118 non-destructive data collection methods. For the second stage, a duplicate transect of cuboid samples was collected from the
119 middle of the core to allow non-destructive data analysis at a higher resolution on one set of the subsampled cubes. As seen in
120 Figure 1, this resulted in the cuboids flanking either side of the MSCL and CT results which were collected from a central
121 transect on the half-core samples.

2.2 Industrial Micro Computerised Tomography

123 Micro Computed tomography (μCT) ~~was used to examine the ice, sediment, and gas contents of several permafrost cores and~~
124 ~~cube samples. This method~~ is a non-destructive technique that has been useful in the investigation of geological porous media
125 (Ashi, 1997; Ketcham and Carlson, 2001; Kozaki et al., 2001; Flisch and Becker, 2007; Calmels and Allard, 2004; Van Geet
126 et al., 2005; Tanaka et al., 2010; Nitzbon et al., 2022). This imaging method captures radiograph images through the production
127 of x-rays which pass through a cabinet and are recorded by the detector panel opposite the source. The sample is placed
128 between the source and the detector panel and the resulting relative absorption of the x-rays energy is recorded by the detector
129 panel creating the radiograph image. To collect a 3 dimensional image, a set of two-dimensional X-ray radiographs are
130 collected at multiple angles, and secondly reconstructed to form a 3D image. The final measurement unit, commonly
131 visualized as a histogram, is the linear attenuation coefficient, which depends on both the density and the electron density of
132 the material~~The final measurement unit which is commonly visualised in a histogram is the linear attenuation coefficient which~~
133 ~~depends on both the density and the electron density of the material~~ (Ketcham and Carlson, 2001). ~~This study differs slightly~~
134 ~~from earlier permafrost CT studies that report values in Hounsfield units that are common in medical CT studies (eg. Calmels~~
135 ~~et al., 2010). In this study, an internal calibration process is used to convert the primary linear attenuation values derived from~~
136 ~~the CT data directly to density (g/cm²).~~

137 The scans presented here were captured using a helical scan with a Nikon XTH 225 ST cabinet-based industrial
138 computed tomography micro-CT scanner. The system uses an electronically adjustable 225Kv 225W power source (Figure
139 2). This system includes both a tungsten rotating reflection target source and a tungsten fixed reflection target source coupled
140 with a 16-bit 2000x2000 pixel detector capable of a focal spot size range of 3-121 μm depending on the size of the area of
141 interest and size of the object being scanned. The 10 cm diameter frozen permafrost half cores were scanned with the reflection
142 target source at 200 Kv 35 μa with an exposure time of 125 ms and a voxel (3D volume element representing pixel resolution
143 and slice thickness) size of 65 μm. Scan times ranged from 30 to 45 minutes per core, with a maximum height of ~12 cm
144 scanned per core due to vertical stage movement limitations and inclusion of calibration materials. The subsampled cubes from
145 the cores were scanned with the rotating reflection target source at 225 Kv 133 μa with an exposure time of 125 ms and a voxel
146 size of 25 μm. Scan times for the subsampled cubes were 30 minutes per cuboid. The images were reconstructed into three-
147 dimensional grey-scale volumes using the Nikon CT pro 3D software and analyzed using ORS Dragonfly 2022 image
148 processing software (ORS 2021).

Commented [MR9]: Check with gpt, delete one which

Commented [MR10]: Change this with gpt to show that rep (meaning the previous studies)

149 An insulated sample holder was developed for this project to ensure samples remained frozen during CT scanning. Both cubes
150 and cores were housed in the same style of a styrofoam container, however, the internal setup varied due to the size of the
151 sample under investigation. Full cores were taken from a nearby chest freezer and placed vertically into a larger container (12
152 cm inner diameter), with a -80 °C ice pack positioned directly above (Figure 2B and C). In contrast, the cubes were placed in
153 smaller containers (9 cm inner diameter), held in plastic vials beneath a foam divider, and cooled with dry ice on a perforated
154 foam layer to circulate cold air over the sample (Figure 2D). These configurations were tested in advance using internal,
155 surface, and air temperature probes, confirming that both setups maintained sub-zero temperatures for the full scan duration.
156 It should also be noted that full core scans produced partial results due to vertical stage height limitations in the CT scanner.
157 While the scanner can hold samples up to ~30 cm wide by 35 cm high, the maximum scan height depends on voxel resolution
158 and sample width. This limitation was resolved once the cores were subsampled for destructive testing. As a result, for some
159 cores, such as the peat core, it was not possible to compare full vertical data sets across MSCL, CT, and destructive methods.
160

161 **2.2.1 CT Calibration**

162 The linear attenuation coefficient (μ) represents the energy attenuated within a single voxel volume while the voxel population
163 is the population of voxels within a scan volume (Ketcham & Carlson, 2001). By creating a histogram (linear attenuation
164 coefficient vs voxel population) with these values, distributions of relative grey values can be presented. If uncalibrated, the
165 resulting grey values observed in the histogram of a CT scan appear as linear attenuation coefficients. The medical field has
166 developed methods for converting linear attenuation coefficients to Hounsfield units and as a result, the Hounsfield unit has
167 become commonly used in CT research (Hounsfield, 1973; Wellington and Vinegar, 1987; Duliu, 1999; Knoll, 2000; Ketcham
168 and Carlson, 2001; Duchesne et al., 2009). Lee et al., 2015 took it one step further and converted mean Hounsfield unit values
169 to bone mineral density values (mg/cm³) via a linear regression analysis. A similar approach was used in this study by collecting
170 the CT scans with an internal standard of known density (water) later used to calibrate the resulting linear attenuation
171 coefficients into g/cm³ using the Nikon CT Pro 3D software (CT Pro version 5.4). It should be noted that all cores were scanned

172 with ice, water, and aluminum calibration pieces of which water proved to be in closest agreement with destructive analyses.
173 The water and aluminum were located outside of the insulated container during the core scans to avoid freezing. The cube
174 scans had only the water located directly above the cube sample but isolated from the sample and dry ice by insulated foam to
175 minimize the exposure to the cold air temperature within the developed insulated container. The aluminum calibration piece

176 generally underestimated the bulk density while the ice calibration piece resulted in a slight overestimation. Aluminum was
177 chosen for its consistent density of 2.71 g/cm³ representing an upper limit of the expected bulk density within the selected
178 materials. The ice calibration was a 15 ml falcon tube filled and frozen at -5C to minimize expansion issues and bubbles.
179 Overall the water calibration produced the most accurate results apart from ice-poor sediments. The Nikon CT Pro 3D software
180 uses a linear two-point calibration with the first fixed point being air (equal to zero) and the second a user-defined value based

181 on a user-selected pixel population. A representative (local) population of pixels was selected from our water sample in a 2D

182 slice of the scan and informed the expected average target value (1 g/cm^3). This results in displaying grey values in g/cm^3.

183 These densities can then be presented in a histogram, the shape of which reflects the volumetric content of the components in

184 the sample (Calmels et al. 2010).

2.2.2 Image Processing

186 Image preprocessing usually consists of two main stages; 1) selection of the Region of Interest or (ROI), 2) segmentation. In

187 this study both stages were done using Dragonfly software (ORS 2021). This software enabled us to process the three-

188 dimensional reconstructed X-ray tomographs of the frozen materials to segment, quantify, calculate, and illustrate the cores'

189 physical properties. For the first stage, a series of ROIs were created in the half core CT results down the central vertical axis

190 of the cores to mimic the data collection points of the MSCL as presented in Pumple et al. (2024). Figure 1 displays the relative

191 location of these ROIs which were sized to match the spot size of the gamma-ray at the surface of the core, ~10 mm in diameter.

192 The central point of each ROI was placed 5 mm apart resulting in a significant overlap between adjacent data points, again

193 similar to the data collection process for the MSCL. In this study, all cores were calibrated so the histogram values were

194 displayed in g/cm^3. Following calibration, the histograms served not only as visualization tools but also as a means to extract

195 quantitative information. To extract the frozen bulk density from each ROI, the mean grey values were extracted in calibrated

196 density values (g/cm^3).

197 The second stage, segmentation or the ability to differentiate materials, depends on their respective linear attenuation

198 coefficients, meaning materials with divergent densities and/or atomic numbers are easier to differentiate (Kyle and Ketcham,

199 2015). Analysing a multi-modal histogram of a CT image is straightforward for material differentiation while materials with

200 similar unimodal density distributions may appear as a single peak in the histogram (Wang et al., 2024). In addition to the

201 relative density of the scanned materials, the image resolution or voxel size also directly impacts the image segmentation

202 process. The voxel size can impact the image segmentation through the partial volume effect which relates directly to the

203 resolution or voxel size of the scan and for geological samples, to grain size, minimal pore size, and organic content (Soret et

204 al., 2007; Nitzbon et al., 2022).

205 In this study, an automatic image thresholding method named "Otsu " was used. The algorithm of this method, proposed by

206 Nobuyuki Otsu (1979), performs automatic clustering-based image thresholding, assuming that there are two classes of pixels

207 which are "*foreground*" and "*background*" pixels of the image. The optimum thresholding is calculated by distinguishing the

208 two classes so that the minimum class variance is obtained (Kumar and Tiwari, 2019). This method was applied to the selected

209 regions of interest from stage one to differentiate sediment and ice. In each image processing step, we tried to isolate the

210 materials within our scans based on density and slowly slice away the lighter density portion (ice) until we are certain we have

211 collected the target material range (often a mixture of ice and sediment). Figure 3 shows the ice (less dense material) being

212 segmented from the surrounding sediment through multiple image processing steps using the Otsu method where only the

Commented [MR13]: Ref?

213 background (less dense) portion of the previous step is added to the final result. This approach shows that applying the first
214 image processing step will mainly extract the visible ice while using multiple Otsu analyses additional lower-density ice-rich
215 mixtures (mainly pore ice) are extracted, e.g., the area shown inside the red circle of Figure 3B-D. Note that all the above
216 mentioned segmentation steps can also be done by visual inspections instead of automatic thresholding method but it can vary
217 significantly between users, leading to inconsistent results.

218

2.3 Physical Density Measurements

220 Ground-ice content is typically expressed either as the *gravimetric moisture/ice content* (the ratio of the mass of the ice in a
221 sample to the mass of the dry sample) or the *volumetric moisture/ice content* (the ratio of the volume of ice in a sample to the
222 volume of the whole sample) (Van Everdingen, 1998). Ex~~while~~ excess ice refers to the amount of ice in the soil that exceeds
223 the volume of the pore space in the unfrozen state (Subcommittee on Permafrost., 1988). Similar to thaw-strain measurements
224 in geotechnical investigations (Crory, 1973; Shur, 1988; Pullman et al., 2007; Kanevskiy et al., 2012), Kokelj and Burn (2003)
225 and O'Neill and Burn (2012) both applied a method for destructively extracting excess ice content measurements from frozen
226 samples. This method includes the complete thaw, homogenization, and settling time of the sample to extract the supernatant
227 water content and estimate excess ice content. Their method does not require measurement of frozen sample volume since the
228 volumes of sediment as well as the supernatant water should be recorded from the graduated beakers containing the samples
229 once completely thawed. The excess ice content (E_i) of the samples can then be estimated by the equation (Kokelj and Burn,
230 2003):

231 $$(Ei) = \frac{(Wv*1.09)}{(Sv+Wv*1.09)} * 100 \tag{1}$$

232 where Wv is the volume of supernatant water (cm^3), multiplied by 1.09 to estimate the equivalent volume of ice, and Sv is the
233 volume of saturated sediment (cm^3).

234 This study takes an approach similar to Kokelj and Burn (2003) in that the supernatant moisture content is
235 destructively assessed in order to calculate excess ice content. However, since the volume of soil samples was precisely
236 measured through the following steps (Pumple et. al, 2024), volumetric ice contents were also measured.

237 To independently assess density and ice content measurements and also being able to perform scans at higher
238 resolutions, the cores were subsampled as 2x2x4cm cubes. The subsampling process was done in a walk-in freezer maintained
239 at −7°C. The initial step involved removing material from the outer edges of the whole core that might have thawed during
240 coring or been affected by sample storage. Core segments were split lengthwise with a rock saw equipped with a 35 cm
241 diameter diamond-cutting wheel. Cuboid aliquots were cut from one half of the split core, while the other half was retained as
242 an archive. The rounded edges were removed from the half core to expose an internal slab. For this study, a duplicate set of
243 cuboids was obtained by cutting the internal slab in half. Approximately 3 cm³ aliquots were subsampled from the cores for
244 samples with low ice contents to ensure that the cuboids did not fracture or disintegrate during sampling. Digital callipers

Commented [MR14]: Check gpt, can I still keep while in the new sentence?

Commented [MR15]: Ref?

245 (±0.01 mm) and a digital analytical balance (±0.01 g precision) were used to measure physical dimensions and mass,
246 respectively, to calculate the frozen bulk density. The cuboids were then thawed at room temperature for 24 hours in glass
247 beakers covered with Parafilm to minimize evaporative loss. Excess moisture was removed from the beakers containing the
248 thawed samples, and the sample weight was recorded again to calculate excess moisture content. The cuboids were then dried
249 in an oven for 24 hours at 105°C and reweighed to determine both volumetric ice content and gravimetric moisture content.
250 Finally, the remaining dried material was heated at 550°C for 4 hours to determine the percent organic content via loss on
251 ignition. High organic content could result in water absorption by soil matrix upon thaw and more complexity in the
252 ~~measur~~measurements~~ing~~ of excess ice contents.

253 Because in some soils, such as peat, excess ice will be absorbed by the soil skeleton upon thaw (Johnston, 1981), the
254 Kokelj and Burn method was adjusted for samples with high organic contents by applying a slight pressure on the thawed cube
255 and extraction of the released water. Additionally, the organic content of each sample was measured via loss on ignition (LOI)
256 (Heiri et al., 2001). The *cuboid* method, described by Bandara et al. (2019), is similar to other volumetric and gravimetric
257 methods used to measure bulk density and ice content, but takes advantage of the frozen state of the material which allows for
258 a greater accuracy of volume measurement. Processing is undertaken in a walk-in freezer following methods outlined in
259 Pumple et al. (2024).

260 **2.4 Multi Sensor Core Logger (MSCL)**

261 The PACS Laboratory MSCL is a floor-mounted, automated logging system, manufactured by Geotek, which can be used to
262 analyse whole or split cores. This core logger is equipped with two magnetic susceptibility instruments, a line-scan camera,
263 and a Caesium-137 (^{137}Cs) gamma source and detector which provides measurements of gamma attenuation. Pumple et al.
264 (2024) provides additional details on the methods used for the MSCL data collection and calibration. This analysis yields key
265 physical parameters such as frozen bulk density and volumetric ice content, derived from gamma attenuation measurements
266 combined with soil density estimates and established equations (Lin et al., 2020). We used the density and volumetric ice
267 content results reported by Pumple et al. (2024) as an established non-destructive reference technique to validate and compare
268 with our own ice content estimations.~~The combination of the frozen bulk density results from the gamma attenuation, an~~
269 ~~estimation of soil density, and the equation for volumetric ice content (following Lin et al., 2020) can be used with the MSCL~~
270 ~~to estimate ice content non-destructively (Pumple et al., 2024).~~
271

272 **3 Results and Discussions**

273 Figures 4 A and B show one slice of a small ROI and its histogram from 5 different cores of this study. The differences
274 in the shapes of the histograms are due to the different sediment densities. The diamicton core has the highest sediment density

Commented [MR16]: Add one sentence to show which information is obtained from this analysis. The text only refers to methodology and provides the full reference, but would be good to give the reader the information on the parameters obtained from this method.

275 and a bimodal histogram in which the first mode represents ice and the second is related to the sediments and clasts. Whereas

276 in the other cores, ice and sediment appear as a single mode. Image segmentation of these slices using the Otsu method resulted

277 in the differentiation of 5 different classes of ice/sediment ratios on the basis of their relative densities; air, low ice or sediment-

278 poor ice, high ice or sediment-rich ice, low sediment or ice-rich sediments, and high sediment or ice-poor sediments or clasts

279 shown in Figures 4 B and C. Low ice comprises primary visual or excess ice, while high ice mainly results from extraction of

280 pore ice or ice proximal to sediment (sediment-rich ice). It should be noted that the pore ice inclusions within the mineral soil

281 matrix are often smaller than the spatial resolution of the CT and the resulting grey value of a voxel is related to the mixture

282 composition of low-density ice and high-density mineral grains. This phenomenon, called partial volume effect, is the main

283 reason why the high ice appears denser. Low sediment and high sediment categories differentiate ice-rich sediments from

284 sediments with lower and higher densities, respectively. Figure 5a-f illustrate the image segmentation results for the whole

285 diamicton core, highlighting these distinctions. Low sediment and high sediment are also differentiating ice-rich sediments and

286 sediments with lower and higher densities, respectively. Figure 5 illustrates the image segmentation results in the whole

287 diamicton core.

3.1 Core Results

291 Physical properties of the permafrost samples, determined from the cuboids, including frozen bulk density, volumetric (VIC)

292 and excess ice contents (EIC), and organic contents are plotted versus the depth of the cores and shown as B, C, and D in

293 Figures 6-10, respectively. The vertical cross-section photo of the core (A) is also presented in these figures. The non-

294 destructive CT results for VIC, EIC, and bulk density for each core are then compared to both the destructive cuboid and non-

295 destructive MSCL results using an average root mean square error (RMSE) (Table 2).

3.1.1 Ice-rich Silt Core (BH18-211):

297 Figure 6 shows the destructive (cuboid) and non-destructive (CT and MSCL) results of the ice-rich silt core, illustrating that

298 the CT frozen bulk densities are in strong agreement with both the cuboid (RMSE = 0.12 g/cm^3) and MSCL (RMSE = 0.14

299 g/cm^3) results. This core has a high organic content (8-19% organic), micro-lenticular and layered cryostructures, and 66%

300 silt. Cuboid physical EIC and VIC measurements range from 19-34% and 68-76%, respectively, while the CT EIC and VIC

301 estimates range from 20-68% and 32-74% at the same depths where cuboid measurements were collected. The 65 μm EIC

302 (redline in Figure 6C) shows good accordance with the cuboid EICs (RMSE = 9%) apart from the ice layer where the cuboid's

303 relatively low sample resolution results in an averaging out of the ice content across the ice layer. The 65 μm CT-VICs (black

304 line in Figure 6C) illustrate the resolution limitation in extracting the pore ice of this sandy silt core while the 25μm VICs

305 shown as black cubes in the same plot tackle this limitation and agree well with VICs extracted from the Cuboid method

306 (RMSE = 7%). The MSCL VICs follow the same trend as the cuboid data (Fig 6-C) but consistently tend toward lower values

307 in the ice-poor regions.

3.1.2 Transition Core (BH12F-138):

Figure 7 shows the results of the transition core from both destructive (cuboid) and non-destructive (CT and MSCL) methods, illustrating a sharp boundary between an ice-rich silty peat, containing massive and rare crustal cryostructures, and an ice-poor inorganic silt with a mainly micro-lenticular cryostructure. The organic content of the core's top section, ranging from 53-71%, highlights this transition (Figure 7D). Cuboid physical EIC and VIC measurements range from 6-28% and 64-88%, respectively, while the CT EIC and VIC estimates range from 9-33% and 42-95% at the same depths where cuboid measurements were collected. This figure also shows that the CT bulk density results are in strong agreement with both the cuboid (RMSE = 0.13 g/cm^3) and gamma attenuation data (RMSE = 0.06 g/cm^3) in agreement with the results reported by (Pumple et al., 2024). The 65 µm EIC results (red line in Figure 7-C) follow the cuboid results (RMSE = 5%) in the silty section. The 65 µm VIC (black line in Figure 7C) resolves more than 50% of pore ice, while the higher resolution (25 µm, black cubes in Figure 7C), estimates up to 100% (RMSE = 3%).

3.1.3 Diamicton Core (BS19-3-6):

Figure 8 illustrates the destructive (cuboid) and non-destructive (CT and MSCL) results of the diamicton core. This ice-rich diamicton contains both suspended and crustal cryostructures and more than 50% silt (Table 1). Overall the bulk density and ice measurements from CT display high concordance with the gamma attenuation (RMSE = 0.14 g/cm^3), and cuboid (RMSE = 0.14 g/cm^3) methods (Figure 8). Cuboid physical EIC and VIC measurements range from 30-50% and 48-66%, respectively, while the CT EIC and VIC estimates range from 22-57% and 36-77% at the same depths as the cuboid measurements. The 65 µm EIC results (red line in Figure 8C) follow the cuboid results (RMSE = 8%). The only point where the datasets differ notably is at 2-4 cm depth where the MSCL values shifts towards lower densities due to the core's lateral heterogeneity while the CT density still lines up well with the cuboid results. The ice contents of this cube are also much lower than CT and MSCL results. This is due to the collection procedure of the cubes which were just off-center to accommodate a duplicate run of cubes down the middle of the core for CT imaging and destructive measurements (as shown in Figure 1). This single cube highlights the effect of differences in the locations of ROIs between CT/MSCL and the cuboid methods. Moreover, at this depth in the core cuboid sample, there was a clast which resulted in a local density high and lower ice content.

In this core, the 65 µm VICs agree well with the cuboid-VICs, MSCL (RMSE = 4%) ice contents, and 25 µm cube scan results (RMSE = 3%) while in the transition core, the 65 µm VICs underestimated the other VIC results. The difference between the 65 um VIC results and other VIC results for all cores except the diamict could be a result of the sample's grain size as the diamict has high clay content (~18%) relative to the other cores (~8-12%) (Table 1).

3.1.4 Ice-poor Silt Core (BH20B-337):

Figure 9 shows the results of the ice-poor silt core from both destructive (cuboid) and non-destructive (CT and MSCL) methods, illustrating a massive (non-visible) cryostructure within this inorganic silt that highlights the relatively low overall

339 ice content throughout the core. This core has little variability throughout its profile. The CT bulk densities are consistent with
340 both the cuboid (RMSE = 0.14 g/cm^3) and gamma attenuation data (RMSE = 0.14 g/cm^3) (Figure 9). The 65 μm EIC results
341 compare well with the cuboid EIC results (RMSE = 5%) while the 25 μm cube scan ice contents show strong agreement
342 (RMSE = 3%) with the volumetric cuboid ice content estimates. It should be noted that based on the EIC results of 65 μm
343 scans, the core has a small percentage of ice (around 5%) in the form of microstructures beyond the natural pore space within
344 the host sediment. However, upon thawing, the surrounding sediment absorbs the moisture into the available pore space,
345 resulting in no EIC during the destructive analysis.

346 **3.1.5 Peat Core (DH13-589):**

347 Figure 10 illustrates the destructive (cuboid) and non-destructive (CT and MSCL) characterization results of the peat core,
348 with little variability throughout its profile. The core is formed of homogenous organics, with an organic-matrix cryostructure
349 of visible ice within the densely packed peat. The CT bulk density results are similar to both the cuboid (RMSE = 0.05 g/cm^3)
350 and gamma attenuation results (RMSE = 0.03 g/cm^3) (Figure 10). The 65 μm ice content results (39-48% of EIC) are also in
351 accordance with the cuboid excess ice results (RMSE = 4%). The 65 μum and 25 μum VICs are both showing good estimates
352 of VICs (RMSE = 1%). It should be considered that the adjusted method for extraction of supernatant water, using slight
353 pressure to release water from the organic matrix, was applied to the cubes of this core. As it was previously discussed, this
354 pressure will release the excess water that was absorbed by the peat skeleton upon thaw (Johnston, 1981).

355 **3.2 Sensitivity analysis**

356 In this study in order to do a sensitivity analysis and investigate the impact of resolution on the delineation between ice and
357 sediment, repeat scans were conducted on the same cube. Initially, the half cores (10 cm diameter) were scanned with a 65 μm
358 voxel size. This was due to the physical size (width) of the imaging window. The smaller size of the cubes, however, presented
359 an opportunity to collect data from the same material but at a resolution of 25 μm. Some of the cubes were also scanned at the
360 same 65 μm resolution as the half cores to make a direct comparison. Figure 11 shows the same slice location and orientation
361 from the same cube at two different resolutions.
362   A ROI, shown as a red square in Figure 11, was then selected in each CT-scanned cube to make a direct comparison
363 between the delineated (Otsu split) ice contents from image processing and the ice contents determined from the destructive
364 cuboid analysis of the corresponding cube sample. As reference points, the cuboid ice content results for this cube were as
365 follows; 22% excess ice and 65% volumetric ice contents. Figure 12 shows the collected data from repeat image processing
366 steps using the Otsu method of each cube scanned at both 25 μm and 65 μm resolutions as well as the cuboid results. The initial
367 image processing steps for both the 25 μm and 65 μm scans closely capture the expected value of the EIC. However, only the
368 25 μm cube captures a representative value relative to the cuboid data for the measured volumetric ice content. This value is
369 reached after 6 image processing steps using the Otsu method. These results illustrate the capability of 25 μm resolution for

370 better extracting trapped ice inside pore spaces of this sandy silt sample which could be due to the smaller size of pores than
371 the resolution. The nature of the curve suggests that VIC cannot be delineated from the 65 μm resolution scans however EIC
372 is possible.

373 Additionally, there is an observable increase in the amount of pore space or gas captured in the 25um resolution
374 relative to the 65um. This difference highlights the 25um scan's increased potential to capture, and as a result segment, the
375 different components within the scanned material.

3.3 Comparison of CT and Cuboid Density and Excess Ice Results:

377 Segmentation of the CT images using the Otsu method allows comparison of CT-derived bulk densities, excess ice, and
378 volumetric ice contents with estimates from the cuboid method at similar resolution. We completed these comparisons at 65
379 μm and 25 μm (Figures 13, 14 and 15). ~~These figures display~~ revealing a good agreement for density, excess ice, and
380 volumetric ice measurements with RMSE of 0.12 g/cm^3, 6%, and 3%, respectively. Additionally, the CT results compare well
381 with the MSCL results for both density and VIC with RMSE's of 0.08 g/cm^3 and 7%, respectively (Figures 16 and 17). The
382 differences between the estimated EICs from CT image processing (65 μm-whole core) and the measured ones from the cuboid
383 method are due to the differing resolutions, i.e., 0.5 cm for CT and 2 cm for the cuboid method, as well as the different locations
384 of the regions of interest (previously described in section 2.2). The strong accordance of the VICs highlights the opportunity
385 for higher resolution scans to estimate pore ice.

3.4 Comparison of Non-destructive Methods:

387 The results of this study show strong agreement between the two non-destructive methods: CT and MSCL and highlight the
388 importance of continued development and refinement of non-destructive methods for extracting physical properties from
389 permafrost materials.

390 The presented CT method allows for whole core high-resolution (65 μm) three-dimensional imaging of cores,
391 measurement of bulk density and estimation of excess ice contents at a desired scale. This contrasts with MSCL which is
392 restricted to a fixed data collection transect down the center of the core (~ 1cm wide) with a maximum sample resolution of ~
393 0.5 cm, high resolution (25 μm) 2-dimensional half-core images and currently provides only volumetric ice estimates, and no
394 direct estimates of excess ice. The CT method is capable of estimating volumetric ice contents but requires cores to be
395 subsampled to a smaller size (2x2x4 cm cube) to allow for finer resolution scans (25 μm).

396 It is worth noting that the MSCL provides a more rapid method for collecting bulk density and volumetric ice content
397 estimations in comparison with the CT method. However, in addition to bulk density and volumetric ice content estimations,
398 the CT method can provide direct estimates of excess ice content. Visible ice can be segmented and isolated from the remaining
399 sediment and pore ice when scanning split cores at 65 μm voxel size, allowing the opportunity to better estimate EIC values
400 compared to MSCL methods. Therefore, in terms of a non-destructive method for identifying and quantifying excess ice within

401 permafrost cores the CT method provides a more robust approach although the image processing and acquisition costs are
402 significantly greater.
403
404 **4 Conclusions**
405 This study investigated the application of high-resolution industrial CT scanning as a non-destructive method to tackle the
406 limitations of traditional destructive methods (e.g., visual acuity, poor reproducibility, and low resolution) in permafrost
407 characterization. Investigations were done by systematically logging permafrost cores, visualising cryostructures, measuring
408 bulk density, and estimating volumetric and excess ice contents, independently. Five permafrost cores, representing common
409 materials encountered in permafrost regions, were scanned at voxel sizes of 65 and 25 μm. A new calibration method was used
410 to extract real densities in g/cm^3 directly from CT images. Image segmentation results using Otsu automatic image thresholding
411 method illustrated the effectiveness of this method in generating robust segmentation results while the visual inspection method
412 has its own drawbacks, e.g. inspector's visual acuity and poor reproducibility.
413 The initial identification of different materials from CT images showed 3 classes; air (gas), ice, and sediments while image
414 processing steps of the scans (using Otsu method) illustrated significant density differences in ice and sediment classes. Image
415 segmentation results using multiple image processing steps showed visual/excess ice as a lower density relative to the pore ice
416 and delineated two sediment classes based on densities.
417   Since manual and visual thresholding is subject to operator experience and judgement and also not applicable in
418 images with unimodal histograms related to materials with close densities (organic materials and ice), an automatic
419 thresholding technique was used in this study to generate more consistent results.
420   Comparison of the image processing results and extracted physical properties of 5 permafrost cores were validated
421 against a destructive method (cuboid) and MSCL non-destructive method. The results showed strong agreement between these
422 three methods (CT and cuboid) considering their differing resolutions and regions of interest with overall average RMSE's of
423 3%, 6% and 0.12 g/cm^3 for VIC, EIC and density, respectively. This agreement demonstrates the applicability and reliability
424 of non-destructive methods in tracking physical and cryostructural details of permafrost cores and producing replicable, cost-
425 effective measurements. A sensitivity analysis of the impact of differing resolutions on the delineation between ice and
426 sediment showed that higher resolution scans generate more accurate VICs while the lower resolution scans are still sufficient
427 for estimation of EICs and a rough estimation of VICs.
428   The proposed approach of this study will help build more robust permafrost datasets and strengthen future permafrost
429 research efforts in mapping permafrost properties and the distribution of excess ice and predicting thaw settlement. It also
430 presents an opportunity to develop methods to extract more information from existing datasets based on an acute understanding
431 of the relations between key physical permafrost properties. The next steps can be followed by improving our understanding
432 and techniques of scanning permafrost as well as using machine-learning-based image segmentation methods to generate
433 datasets and explore the relations between physical permafrost properties.

Author contribution

MR, JP, DF, and JH planned the project; MR, JH, and JP developed the methods; MR, JH, and JP performed the measurements; MR and JH analyzed the data; MR, JP and JH wrote the manuscript draft; MR, JP, JH, and DF reviewed and edited the manuscript.

Competing interests

The authors declare that they have no conflict of interest.

Acknowledgements

The authors would like to thank Evan Francis who helped with sample preparation in earlier experiments. We would also like to thank Nikon Metrology for the support and constructive feedback they provided throughout the project. Casey Buchanan is thanked for collecting the diamict sample used in this study.

Financial support

This research was supported by the NSERC funded Permafrost Partnership Network for Canada (PermafrostNet) and NSERC Discovery grant to Duane Froese. Laboratory infrastructure for the Permafrost Archives Laboratory was funded by Canadian Foundation for Innovation, Government of Alberta, and University of Alberta.

References

Ashi, J., Computed tomography scan image analysis of sediments, in Proc. ODP, Sci. Results, edited by Shipley, T. H., Y. Ogawa, P. Blum, and J. M. Bahr, 156, 151–159, 1997.

Bandara, S., Froese, D. G., St. Louis, V. L., Cooke, C. A., and Calmels, F.: Postdepositional Mercury Mobility in a Permafrost Peatland from Central Yukon, Canada, ACS Earth Sp. Chem., 3, 770–778, https://doi.org/10.1021/acsearthspacechem.9b00010, 2019.

Brown, J., Ferrians, O., Heginbottom, J., and Melnikov, E. S.: Circum-Arctic map of permafrost and ground-ice conditions, https://doi.org/10.3133/cp45, 1997.

Cai, L., Lee, H., Schanke Aas, K., and Westermann, S.: Projecting circum-Arctic excess-ground-ice melt with a sub-grid representation in the Community Land Model, Cryosphere, 14, 4611–4626, https://doi.org/10.5194/tc-14-4611-2020, 2020.

Calmels, F. and Allard, M.: Ice segregation and gas distribution in permafrost using tomodensitometric analysis, Permafr. Periglac. Process., 15, 367–378, https://doi.org/10.1002/ppp.508, 2004.

460 Calmels, F. and Allard, M.: Segregated ice structures in various heaved permafrost landforms through CT Scan, Earth Surf.
461 Process. Landforms, 33, 209–225, https://doi.org/10.1002/esp.1538, 2008.

462 Calmels, F., Clavano, W. R., and Froese, D. G.: Progress on X-ray computed tomography (CT) scanning in permfrost studies,
463 in: GeoCalgary 2010 : the 63. Canadian geotechnical conference and 6. Canadian permafrost conference, Calgary, AB
464 (Canada), 12-15 Sep , 1353–1358, 2010.

465 CT Pro version 5.4, Nikon Metrology, Brighton, MI, USA

466 Crory, F.: Settlement associated with the thawing of permafrost, Hanover, New Hampshire, 599–607 pp., 1973.

467 Darrow, M. M. and Lieblappen, R. M.: Visualizing cation treatment effects on frozen clay soils through μCT scanning, Cold
468 Reg. Sci. Technol., 175, https://doi.org/10.1016/j.coldregions.2020.103085, 2020.

469 Duchesne, M. J., Moore, F., Long, B. F., , Labrie, J.: A rapid method for converting medical Computed Tomography scanner
470 topogram attenuation scale to Hounsfield Unit scale and to obtain relative density values. Engineering Geology 103, 100–105,
471 2009.

472 Duliu, O.: Computer axial tomography in geosciences: an overview. Earth-Sci. Rev.
473 48 (4), 265–281, 1999. https://doi.org/10.1016/S0012-8252(99)00056-2

474 Van Everdingen, R. O.: MULTI-LANGUAGE GLOSSARY of PERMAFROST and RELATED GROUND-ICE TERMS,
475 Calgary, 1998.

476 Fan, X., Lin, Z., Gao, Z., Meng, X., Niu, F., Luo, J., Yin, G., Zhou, F., Lan, A.: Cryostructures and ground ice content in ice-
477 rich permafrost area of the Qinghai-Tibet Plateau with Computed Tomography Scanning. Journal of Mountain Science. 18.
478 1208-1221. 10.1007/s11629-020-6197-x, 2021.

479 French, H. M.: The Periglacial Environment, Wiley, 2007, https://doi.org/10.1002/9781118684931

480 Flisch, A., and Becker, A.: Industrial X-ray computed tomography studies of lake sediment drill cores. In: Mees, F., Swennen,
481 R., Van Geet, M., Jacobs, P. (Eds.), Applications of X-ray Computed Tomography. Geological Society, London, Special
482 Publication, 215, pp. 205–212, 2003. https://doi.org/10.1144/GSL.SP.2003.215.01.19

483 French, H., & Shur, Y.: The principles of cryostratigraphy. Earth-Science Reviews, 101(3-4), 190-206, 2010.
484 https://doi.org/10.1016/j.earscirev.2010.04.002

485 Heiri, O., Lotter, A.F. and Lemcke, G., 2001. Loss on ignition as a method for estimating organic and carbonate content in
486 sediments: reproducibility and comparability of results. Journal of paleolimnology, 25(1), pp.101-110.
487 https://doi.org/10.1023/A:1008119611481.

488 Hounsfield, G.N.: Computerized transverse axial scanning (tomography). Part I. Description of system. Br. J. Radiol. 46 (552),
489 1016–1022, 1973. https://doi.org/10.1259/0007-1285-46-552-1016

490 Johnston, G. H.: Permafrost: engineering design and construction, National Research Council Canada. Associate Committee
491 on Geotechnical Research, 1981.

492 Kanevskiy, M., Shur, Y., Fortier, D., Jorgenson, M.T., Stephani, E., 2011a. Cryostratigraphy of late Pleistocene syngenetic
493 permafrost (yedoma) in northern Alaska, Itkillik River exposure. Quaternary Research 75, 584–596
494 http://dx.doi.org/10.1016/j.yqres.2010. 12.003, 2011.

495 Kanevskiy, M., Shur, Y. L., Connor, B., and Dillon, M. R.: Study of the Ice-Rich Syngenetic Permafrost for Road Design
496 (Interior Alaska), in: Tenth International Conference on Permafrost TICOP, 191–196, 2012.

497 Ketcham, R. A. and Carlson, W. D.: Acquisition, optimization and interpretation of X-ray computed tomographic imagery:
498 applications to the geosciences, Comput. Geosci., 27, 381–400, https://doi.org/10.1016/S0098-3004(00)00116-3, 2001.

499 Kokelj, S. V. and Burn, C. R.: Ground ice and soluble cations in near-surface permafrost, Inuvik, Northwest Territories,
500 Canada, Permafr. Periglac. Process., 14, 275–289, https://doi.org/10.1002/ppp.458, 2003.

501 Kokelj, S. V. and Jorgenson, M. T.: Advances in Thermokarst Research, Permafr. Periglac. Process., 24, 108–119,
502 https://doi.org/10.1002/ppp.1779, 2013.

503 Kozaki, T., Suzuki, S., Kozai, N., Sato, S., and Ohashi, H.: Observation of Microstructures of Compacted Bentonite by
504 Microfocus X-Ray Computerized Tomography (Micro-CT), J. Nucl. Sci. Technol., 38, 697–699,
505 https://doi.org/10.1080/18811248.2001.9715085, 2001.

506 Knoll, G.F.: Radiation Detection and Measurement. John Wiley and Sons, New York, 1999.

507 Kumar and Tiwari: A Comparative Study of Otsu Thresholding and K-means Algorithm of Image Segmentation, Int. J. Eng.
508 Tech. Res. , 9, 2019.

509 Kyle, J. R. and Ketcham, R. A.: Application of high resolution X-ray computed tomography to mineral deposit origin,
510 evaluation, and processing, Ore Geol. Rev., 65, 821–839, https://doi.org/10.1016/j.oregeorev.2014.09.034, 2015.

511 Lapalme, C. M., Lacelle, D., Pollard, W., Fortier, D., Davila, A., and McKay, C. P.: Cryostratigraphy and the Sublimation
512 Unconformity in Permafrost from an Ultraxerous Environment, University Valley, McMurdo Dry Valleys of Antarctica,
513 Permafr. Periglac. Process., 28, 649–662, https://doi.org/10.1002/ppp.1948, 2017.

514 Lin, Z., Gao, Z., Fan, X., Niu, F., Luo, J., Yin, G., and Liu, M.: Factors controlling near surface ground-ice characteristics in
515 a region of warm permafrost, Beiluhe Basin, Qinghai-Tibet Plateau, Geoderma, 376, 114540,
516 https://doi.org/10.1016/j.geoderma.2020.114540, 2020.

517 Murton, J. B., & French, H. M.: Cryostructures in permafrost, Tuktoyaktuk coastlands, western arctic Canada. Canadian
518 Journal of Earth Sciences, 31(4), 737-747. DOI:10.1139/e94-067, 1994.

519 Nguyen, T. T. H., Cui, Y.-J., Ferber, V., Herrier, G., Ozturk, T., Plier, F., Puiatti, D., Salager, S., and Tang, A. M.: Effect of
520 freeze-thaw cycles on mechanical strength of lime-treated fine-grained soils, Transp. Geotech., 21, 100281,
521 https://doi.org/10.1016/j.trgeo.2019.100281, 2019.

522 Nitzbon, J., Westermann, S., Langer, M., Martin, L. C. P., Strauss, J., Laboor, S., and Boike, J.: Fast response of cold ice-rich
523 permafrost in northeast Siberia to a warming climate, Nat. Commun., 11, 2201, https://doi.org/10.1038/s41467-020-15725-8,
524 2020.

525 Nitzbon, J., Gadylyaev, D., Schlüter, S., Köhne, J. M., Grosse, G., & Boike, J. (2022). Brief communication: Unravelling the

526 composition and microstructure of a permafrost core using X-ray computed tomography. The Cryosphere, 16, 3507–3515.

527 https://doi.org/10.5194/tc-16-3507-2022

528 O'Neill, H. B. and Burn, C. R.: Physical and temporal factors controlling the development of near-surface ground ice at

529 Illisarvik, Western Arctic coast, Canada, Can. J. Earth Sci., 49, 1096–1110, https://doi.org/10.1139/E2012-043, 2012.

530 Object Research Systems. Dragonfly; Object Research Systems: Montreal, QC, Canada, 2021.

531 Otsu, N.: A Threshold Selection Method from Gray-Level Histograms, IEEE Trans. Syst. Man. Cybern., 9, 62–66,

532 https://doi.org/10.1109/TSMC.1979.4310076, 1979.

533 Pumple, J., Monteath, A., Harvey, J., Roustaei, M., Alvarez, A., Buchanan, C., & Froese, D. (2024). Non-destructive multi-

534 sensor core logging allows rapid imaging, measurement of bulk density and estimation of ice content in permafrost

535 cores. *EGUsphere*,18,, 489-503. https://doi.org/10.5194/tc-18-489-2024

536 Pullman, E. R., Jorgenson, M. T., and Shur, Y.: Thaw settlement in soils of the Arctic Coastal Plain, Alaska, Arctic, Antarct.

537 Alp. Res., 39, 468–476, https://doi.org/10.1657/1523-0430(05-045)[PULLMAN]2.0.CO;2, 2007.

538 Roustaei, M., Pumple, J., Harvey, J., and Froese, D.: Estimating ice and unfrozen water in permafrost samples using industrial

539 computed tomography scanning, in: GeoCalgary 2022, 2022a.

540 Roustaei, M., Pumple, J., Hendry, M. T., Palat, A., and Froese, D.: Freeze-thaw impacts on macropore structure of fiber-

541 reinforced clay by industrial computed tomography scanning, in: GeoCalgary 2022, 2022b.

542 Roustaei, M., Pumple, J., Hendry, M. T., J., Harvey, and Froese, D. (2024) : Effect of freeze–thaw cycles on the macrostructure

543 and failure mechanisms of fiber-reinforced clay using industrial computed tomography, Canadian Geotechnical Journal, 00,

544 1-15, https://doi.org/10.1139/cgj-2023-0136.

545 Shur, Y. L.: The upper horizon of permafrost soils, in: Proceedings of the Fifth International Conference on Permafrost, 867–

546 871, 1988.

547 Soret M, Bacharach SL, Buvat I. Partial-volume effect in PET tumor imaging. J Nucl Med. 2007;48:932–945.

548 Stephani, E., D. Fortier, Y. Shur, R. Fortier, and G. Doré. "A geosys-tems approach to permafrost investigations for engineering

549 applica-tions, an example from a road stabilization experiment, Beaver Creek,Yukon, Canada."Cold Reg. Sci. Technol.100:

550 20–35.https://doi.org/10.1016/j.coldregions.2013.12.006, 2014.

551 Subcommittee, P.: Glossary of permafrost and related ground-ice terms. Associate Committee on Geotechnical Research,

552 National Research Council of Canada, Ottawa, 156, 63-64, 1988. https://doi.org/10.1139/e94-067

553 Tanaka, E. Y., Yoo, J. H., Rodrigues, A. J., Utiyama, E. M., Birolini, D., and Rasslan, S.: A computerized tomography scan

554 method for calculating the hernia sac and abdominal cavity volume in complex large incisional hernia with loss of domain,

555 Hernia, 14, 63–69, https://doi.org/10.1007/s10029-009-0560-8, 2010.

556 Torrance, J. K., Elliot, T., Martin, R., and Heck, R. J.: X-ray computed tomography of frozen soil, Cold Reg. Sci. Technol.,

557 53, 75–82, https://doi.org/10.1016/j.coldregions.2007.04.010, 2008.

558 Wang, S., Yang, P., and Yang, Z. (Joey): Characterization of freeze–thaw effects within clay by 3D X-ray Computed
559 Tomography, Cold Reg. Sci. Technol., 148, 13–21, https://doi.org/10.1016/j.coldregions.2018.01.001, 2018.
560 Wang, Y., Chen, Z., and Wang, G.: Material segmentation in industrial X-ray CT images using histogram-based thresholding:
561 challenges with unimodal and multimodal distributions, Acta Radiol., 65, 901–911,
562 https://doi.org/10.1177/02841851231225418, 2024.
563 Wellington, S.L., Vinegar, H.J.: X-ray computerized tomography. J. Pet. Technol. 39 (8), 885–898,1987.
564 Westermann, S., Langer, M., Boike, J., Heikenfeld, M., Peter, M., Etzelmüller, B., and Krinner, G.: Simulating the thermal
565 regime and thaw processes of ice-rich permafrost ground with the land-surface model CryoGrid 3, Geosci. Model Dev., 9,
566 523–546, https://doi.org/10.5194/gmd-9-523-2016, 2016.
567 Zhang, T., Barry, R. G., Knowles, K., Heginbottom, J. A., and Brown, J.: Statistics and characteristics of permafrost and
568 ground-ice distribution in the Northern Hemisphere 1, Polar Geogr., 23, 132–154,
569 https://doi.org/10.1080/10889379909377670, 1999.

570

571

572

573

574

575

576

577

578 **Table 1: Sampling location and physical properties of cores analyzed in the study.**

579

Core ID	Length (cm)	Classification/ Properties	Collection Location/ Depositional Environment	Clay (%)	Silt (%)	Sand (%)
BH18-211	23	Ice-rich silt	Alaska HWY, Southwestern Yukon, Canada	11	66	23
BH12F-138	16	ice-rich silty peat (top) and ice-poor silt (bottom)	Alaska HWY, Southwestern Yukon, Canada	top 8 bottom 12	top 52 bottom 57	top 40 bottom 31
BS19-3-6	19	Diamicton	Dempster HWY, Central Yukon, Canada	18	51	31

BH20B-337	20	Ice-poor silt	Alaska HWY, Southwestern Yukon, Canada	8	67	25
DH13-589	26	Ice-rich homogenous peat.	Dempster HWY, Central Yukon, Canada	N/A	N/A	N/A

580

581
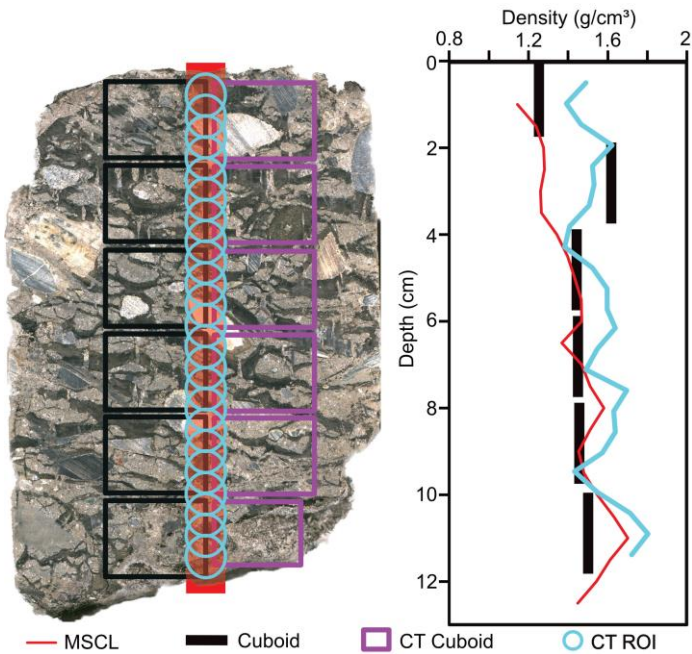
Figure 1: Image of a core highlighting the destructive subsample locations relative to the non-destructive data collection transects (black: subsampled cubes for destructive measurements, purple: subsampled cubes for CT scans)

585

586

587
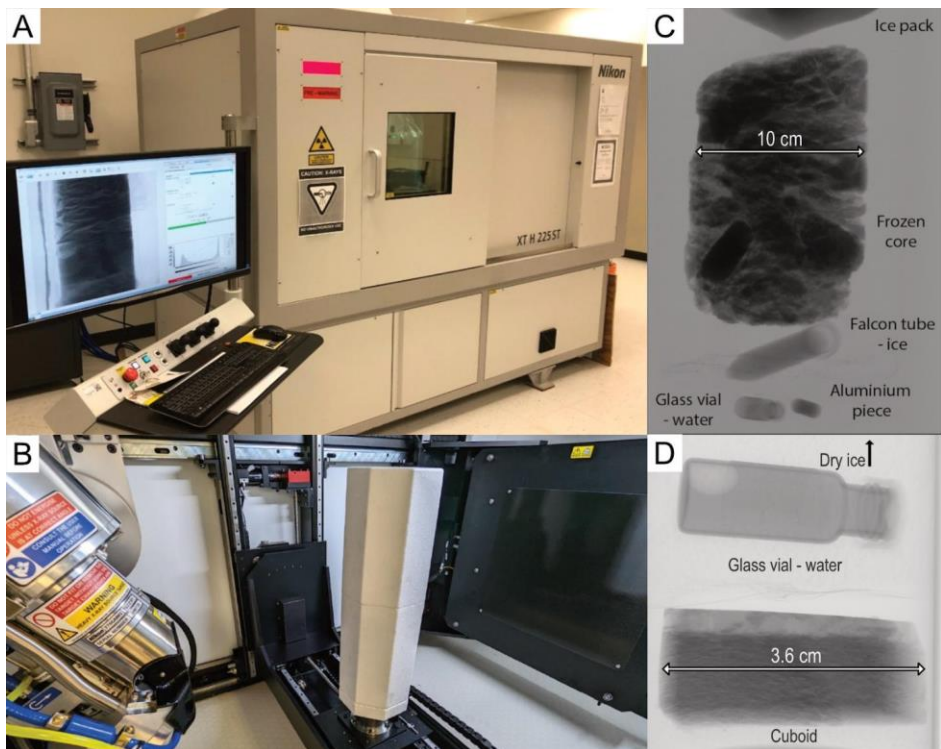
588 **Figure 2: (A) The CT scanner of the PACS Lab.(B) The internal setup for the core scan. (C) X-ray image of the internal setup of the**
589 **core (D) X-ray image of the internal setup of the cube.**

590

591

592

593
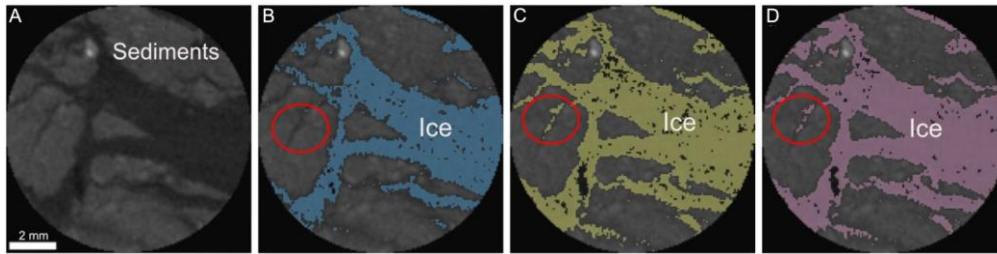
594 **Figure 3: Overview of a slice from ice rich silt core (A) before image processing (B) after the first step, (C) after the second step, and**
595 **(D) after the third step of image processing using the Otsu method.**
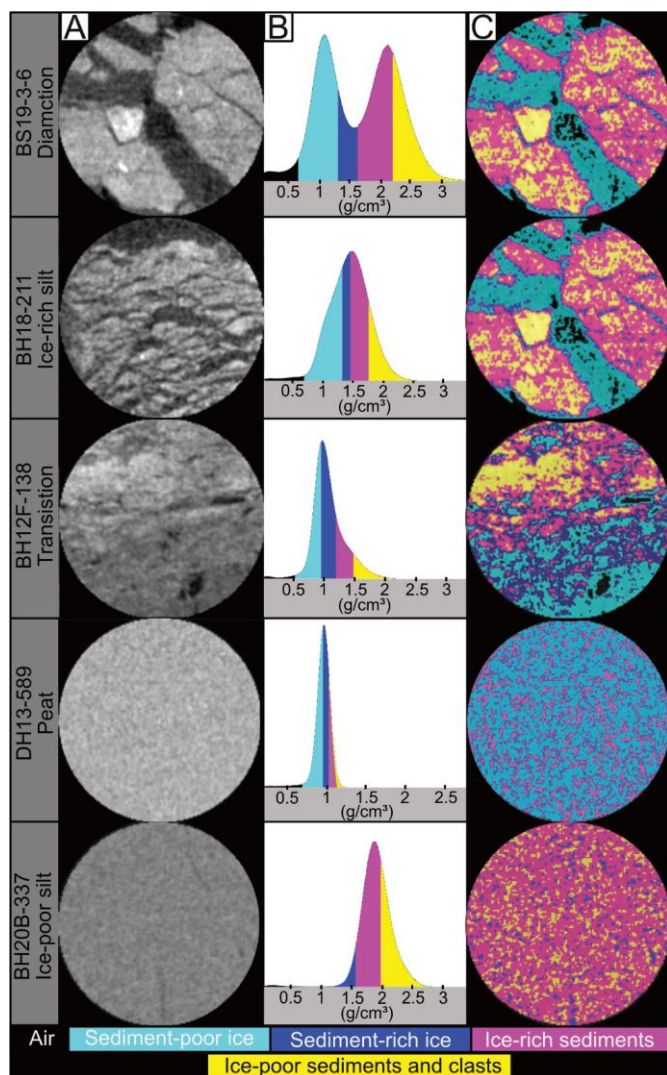
596
597
598 Figure 4: (A) overview of slices from the permafrost cores before image processing (B) histograms, and (C) image segmentation
599 results

Air

Sediment -poor ice

Sediment-rich ice

Ice-rich sediments

Ice-poor sediments and clasts

Increasing density →
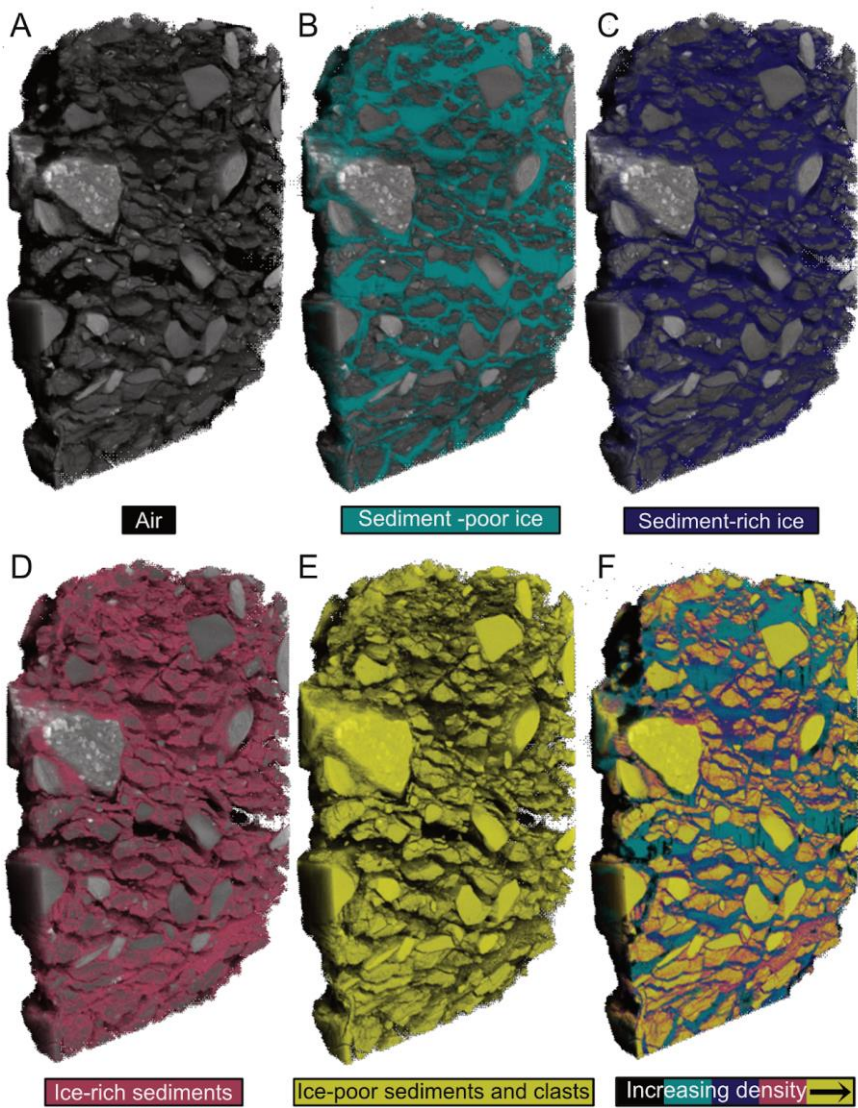
600
601   **Figure 5: Image segmentation results of the diamicton core.**

Table 2: Root mean square error results for the comparison between the CT, Cuboid and MSCL VIC, EIC and density results.

Core ID	RMSE Density CT vs Cuboid (g/cm^3)	RMSE VIC CT vs Cuboid (%)	RMSE VEIC CT vs Cuboid (%)	RMSE Density CT vs Geotek (g/cm^3)	RMSE VIC CT vs Geotek (%)
BS19-3-6	0.14	3	8	0.14	4
BH18-211	0.12	7	9	0.05	8
DH13-589	0.05	1	4	0.03	4
BH12F-138 (top)	0.07	3	7	0.02	11
BH12F-138 (bottom)	0.19	3	2	0.10	10
BH12F-138 (whole core)	0.13	3	5	0.06	10
BH20B-337	0.14	3	5	0.14	3
Overall average	0.12	3	6	0.08	7
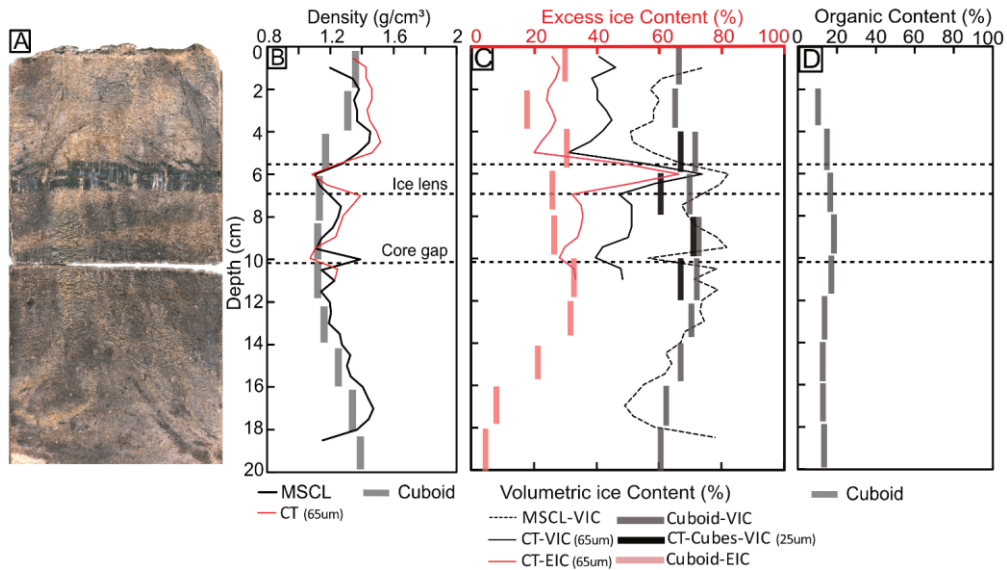
Figure 6: (A) MSCL image of the ice-rich, organic-rich silt core; (B) bulk density; (C) ice contents; (D) organic content distribution in core depth; (E) black and white image of MSCL image with ice highlighted in black.
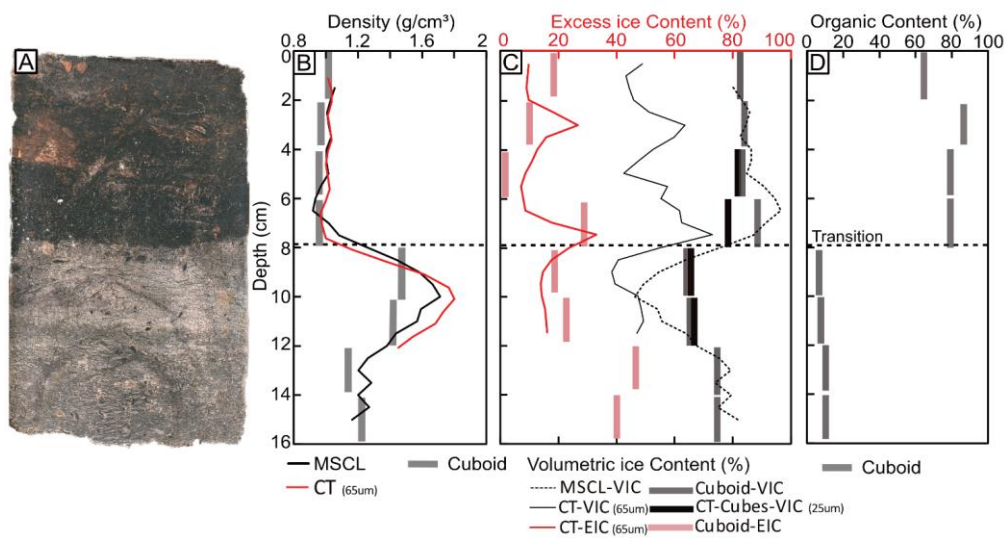
Figure 7: (A) MSCL image of the transition core; (B) bulk density; (C) ice contents; (D) organic content distribution in core depth; (E) black and white image of MSCL image with ice highlighted in black.

612
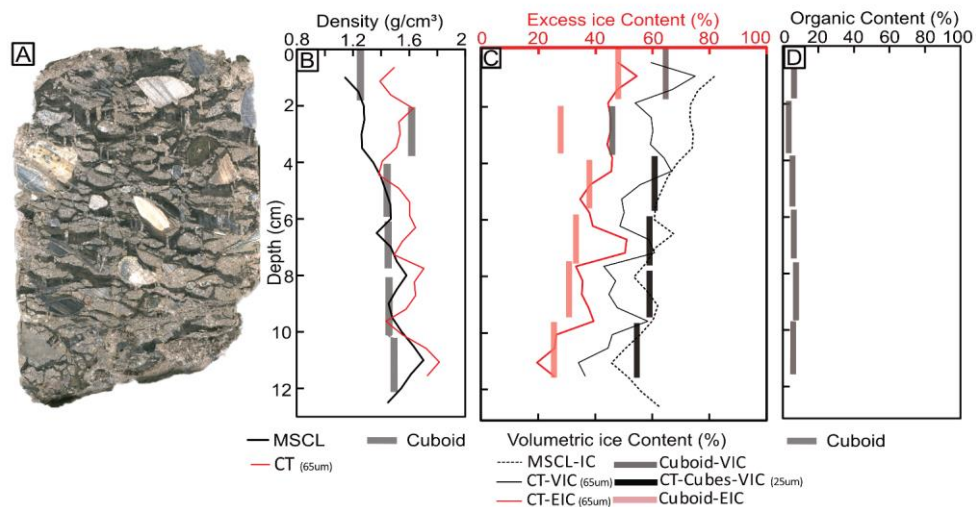
Figure 8: (A) MSCL image of the diamicton core; (B) bulk density; (C) ice contents; (D) organic content distribution in core depth; (E) black and white image of MSCL image with ice highlighted in black.

615

616

617
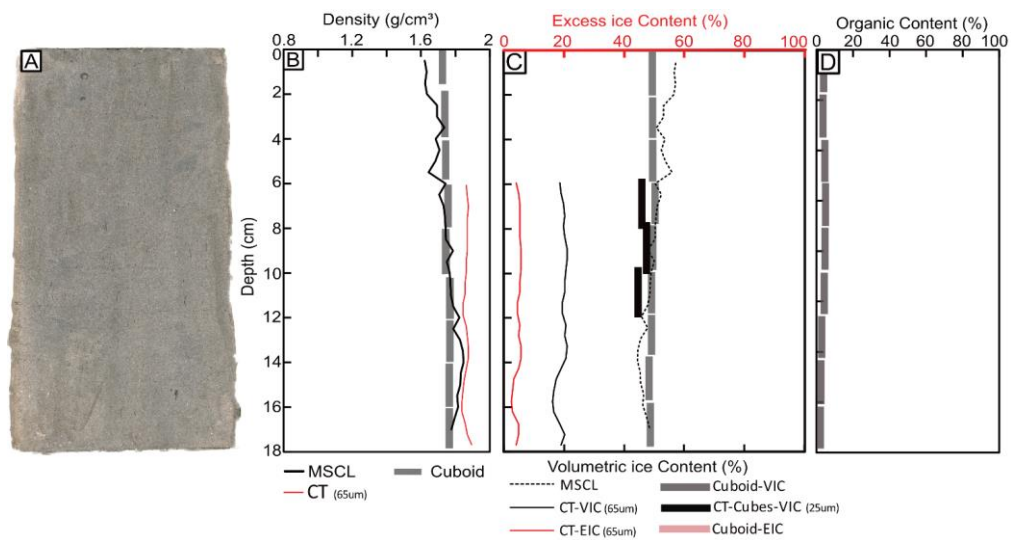
Figure 9: (A) MSCL image of the ice-poor silt core; (B) bulk density; (C) ice contents; (D) organic content distribution in core depth; (E) black and white image of MSCL image with ice highlighted in black.

620
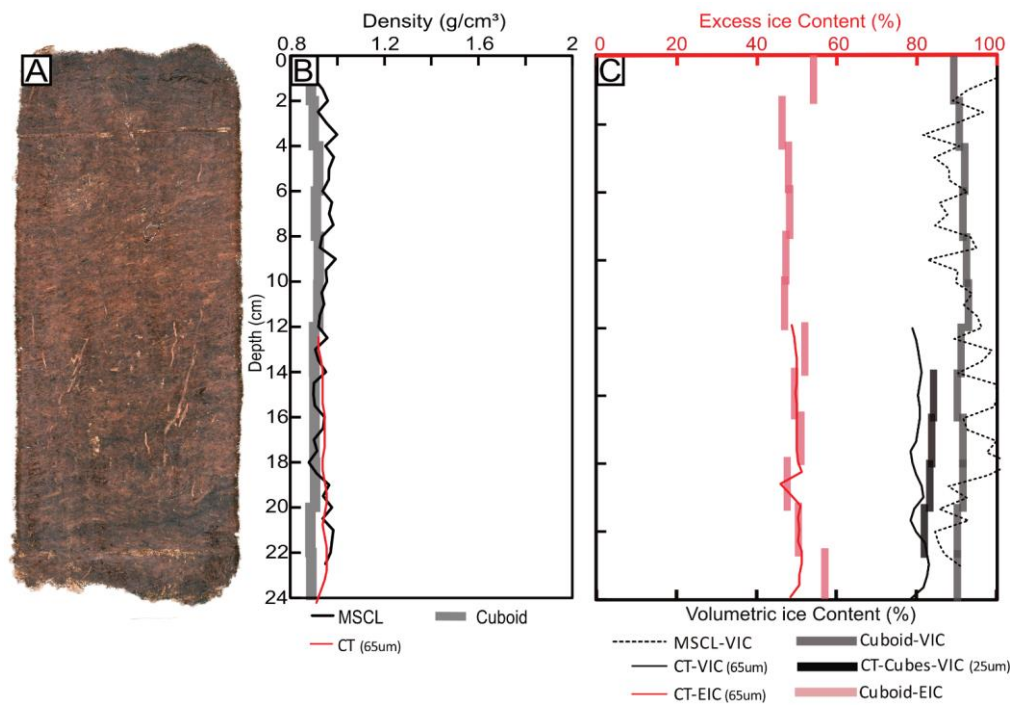
Figure 10: (A) MSCL image of the peat core; (B) bulk density; (C) ice contents; (D) organic content distribution in core depth; (E)
black and white image of MSCL image with ice highlighted in black.
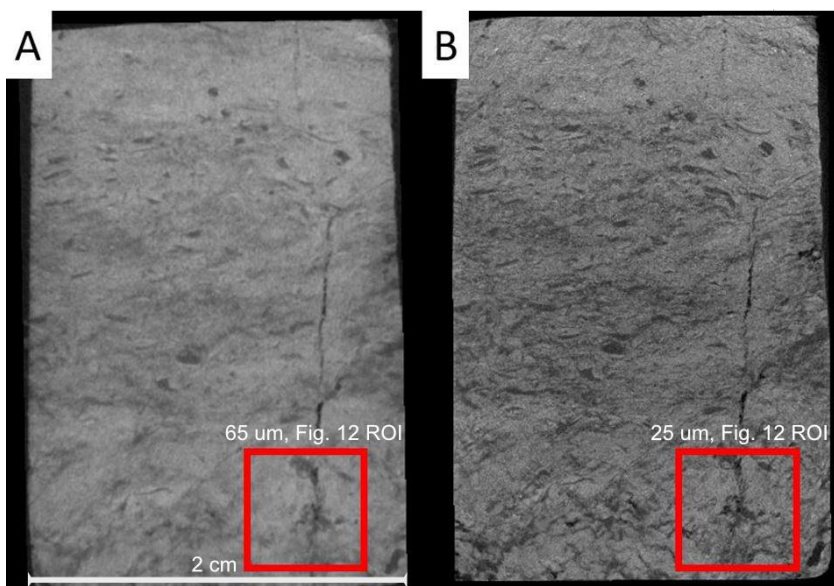
623
624 **Figure 11: CT images of a cube (BH12F-138-10-12 cm) from the transition core at 65 μm (A) and 25 μm (B).**
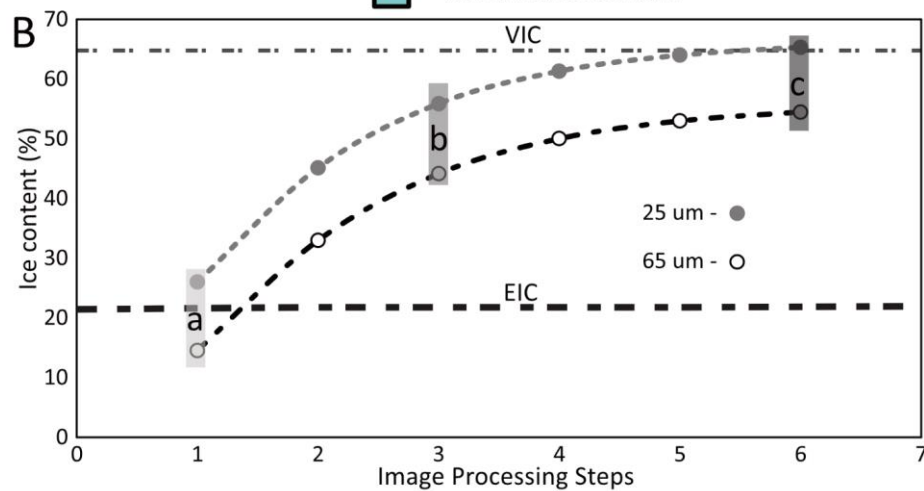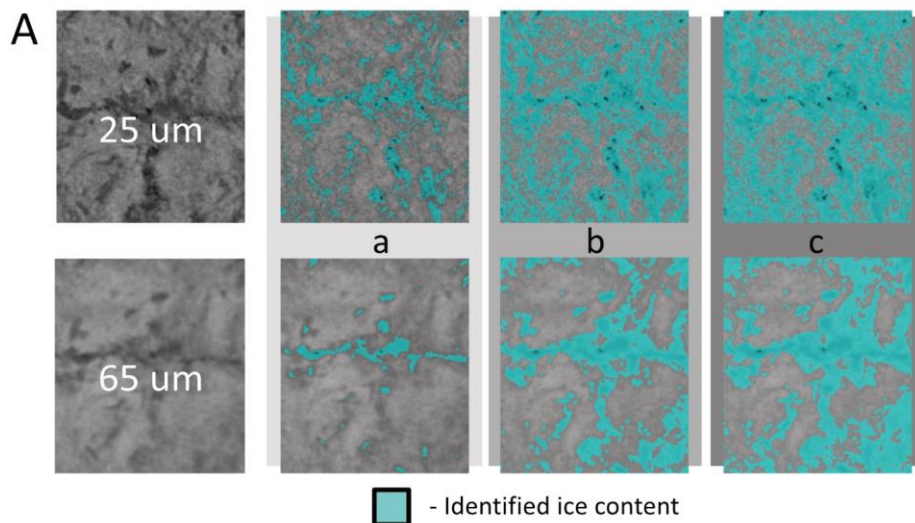
Figure 12: (A) CT ROI's taken from the 65 µm and 25 µm cube scans (BH12F-138-10-12 cm), (B) Identified ice contents at each image processing step using the Otsu split method.

629
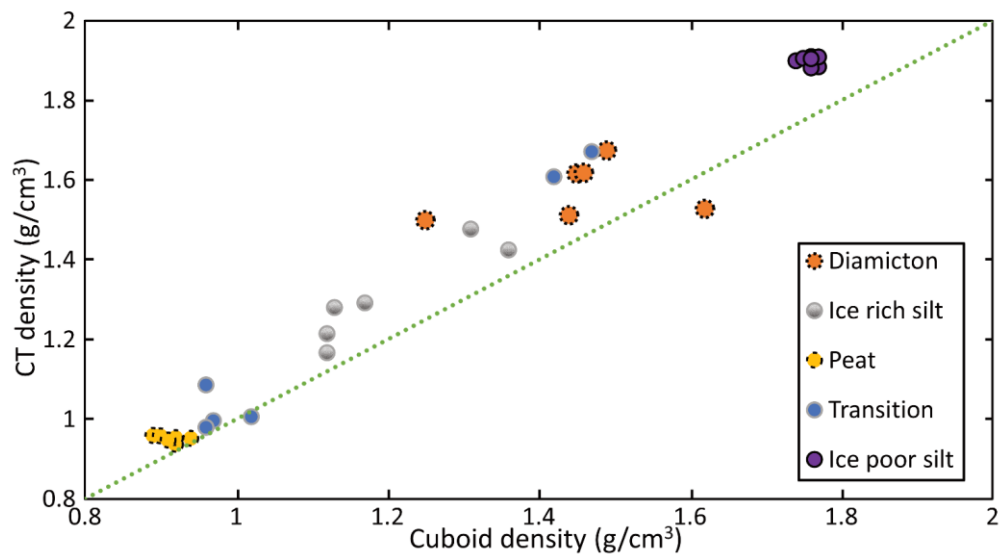
Figure 13: Estimated densities from CT image processing of 65 μm scans vs calculated ones from cuboid method.

631
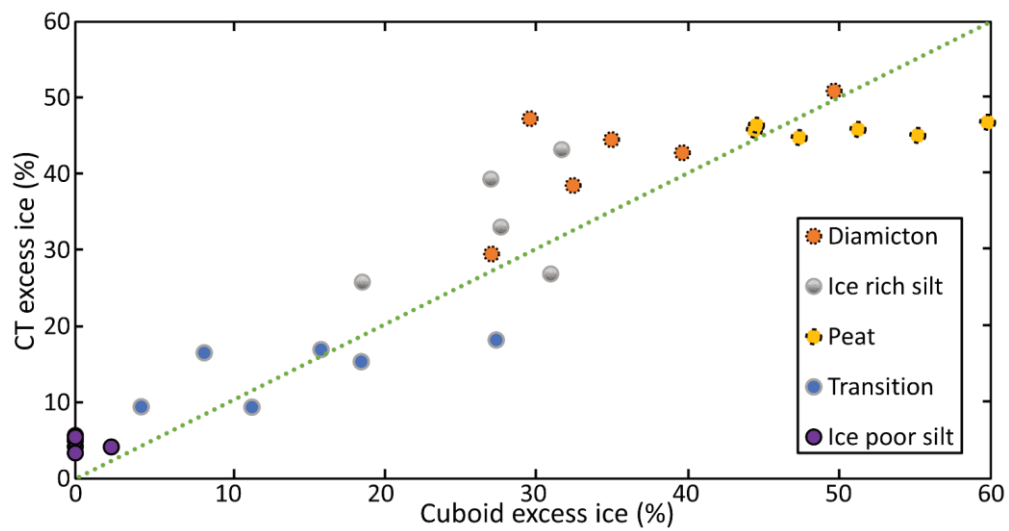
632
633 **Figure 14: Estimated excess ice contents from CT image processing of 65 μm scans vs calculated values from cuboid method.**
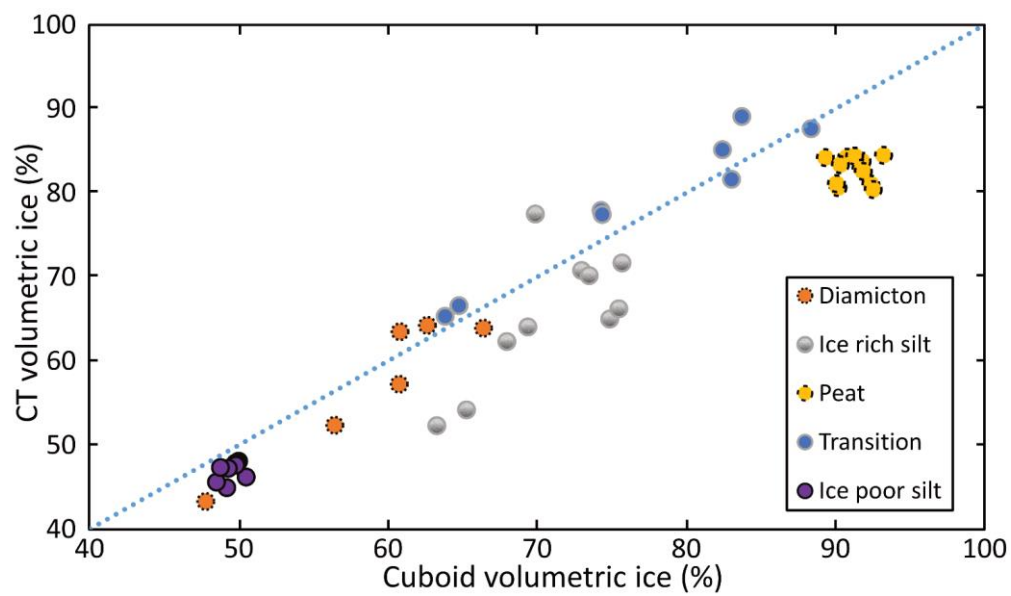
634
635 **Figure 15: Estimated volumetric ice contents from CT image processing of 65 μm scans vs calculated values from cuboid method.**
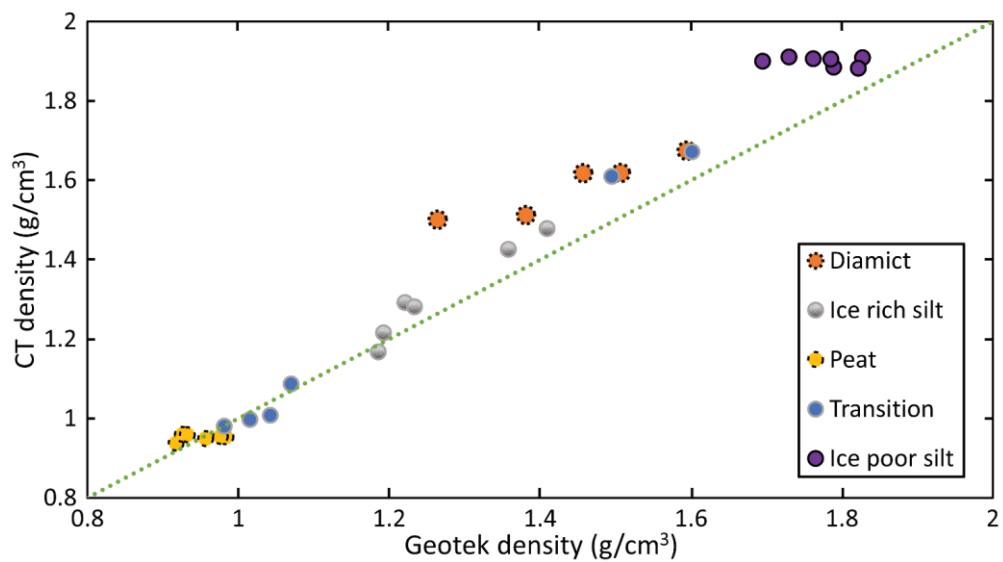
636
637 **Figure 16: Estimated bulk density from CT image processing vs calculated values from MSCL method.**

638
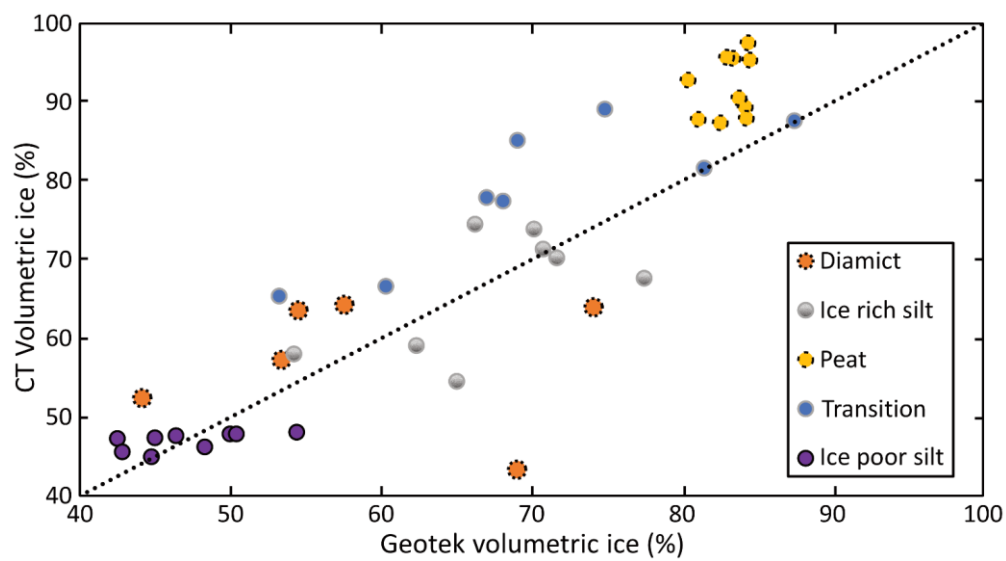
639 **Figure 17: Estimated volumetric ice contents from CT image processing vs calculated values from MSCL method.**

640